

# MICP-L: Mesh-based ICP for Robot Localization using Hardware-Accelerated Ray Casting

Alexander Mock<sup>1</sup>, Thomas Wiemann<sup>3</sup>, Sebastian Pütz<sup>2</sup> and Joachim Hertzberg<sup>1,2</sup>

**Abstract**—Triangle mesh maps have proven to be a versatile 3D environment representation for robots to navigate in challenging indoor and outdoor environments exhibiting tunnels, hills and varying slopes. To make use of these mesh maps, methods are needed that allow robots to accurately localize themselves to perform typical tasks like path planning and navigation. We present *Mesh ICP Localization* (MICP-L), a novel and computationally efficient method for registering one or more range sensors to a triangle mesh map to continuously localize a robot in 6D, even in GPS-denied environments. We accelerate the computation of *ray casting correspondences* (RCC) between range sensors and mesh maps by supporting different parallel computing devices like multicore CPUs, GPUs and the latest NVIDIA RTX hardware. By additionally transforming the covariance computation into a reduction operation, we can optimize the initial guessed poses in parallel on CPUs or GPUs, making our implementation applicable in real-time on a variety of target architectures. We demonstrate the robustness of our localization approach with datasets from agriculture, drones, and automotive domains.

## I. INTRODUCTION

Localization is the task of estimating the state of a mobile robot in a reference coordinate system. It is the foundation for any mobile robot to operate autonomously in a given application environment. In many outdoor scenarios, localization is done via GPS or triangulation with predefined landmarks. However, in many cases, GPS is unreliable or not available at all, therefore other localization strategies have to be considered. Algorithms such as LiDAR-based SLAM have been developed to address this problem. In recent years, such SLAM algorithms have been improved in a way that even robots with low computational resources can estimate their current state in 6DoF while simultaneously mapping their environment in 3D. An increasingly important map representation in the context of SLAM are Truncated Signed Distance Fields (TSDFs) [1]. TSDFs can be transferred easily into 3D triangle meshes to compress the information encoded in the original map. Recently, algorithms have been developed to plan the motion of a robot over the mesh's surface to a given goal [2]. To execute such plans, continuous localization in mesh maps is required.

<sup>1</sup>Knowledge-Based Systems group, Institute of Computer Science, Osnabrück University, Hamburger Straße 24, 49084 Osnabrück, Germany amock@uos.de, joachim.hertzberg@uos.de

<sup>2</sup>DFKI Robotics Innovation Center, Osnabrück branch, Hamburger Straße 24, 49084 Osnabrück, Germany sebastian.puetz@dfki.de

<sup>3</sup>Robotics in Computer Science, Fulda University of Applied Sciences, Fulda, Germany thomas.wiemann@informatik.hs-fulda.de

The DFKI Niedersachsen Lab (DFKI NI) is sponsored by the Ministry of Science and Culture of Lower Saxony and the VolkswagenStiftung



Fig. 1: The Lero agricultural monitoring robot uses MICP-L for localization during mesh-based navigation between beds in a market garden micro-farming environment.

Our paper presents a novel approach called MICP-L<sup>1</sup>, which enables robots equipped with arbitrary range sensors to be localized directly in triangle mesh maps. It is designed to be applicable to robots with varying computational capabilities. For that, MICP-L uses our open-source library Rmagine [3]. In this paper, we contribute

- Robust range sensor to mesh registration via hardware-accelerated ray casting correspondences (RCC),
- Accurate and reliable localization, tested in various real-world domains as shown in Fig. 1,
- Flexible workload distribution to CPU or GPU, enabling application on various hardware platforms,
- Support of arbitrary range sensor configurations and arrays.

## II. RELATED WORK

Generating 3D triangle meshes online [4], even on system-on-chip (SoC) devices [1] and for large scales environments [5]–[8] have become available. Meshes feature a closed surface and can be used for planning and executing paths of autonomously driving robots in unstructured environments [2]. The success of mesh navigation software heavily depends on the robot's ability to frequently and reliably localize itself with relation to the mesh map. In principle, global localization in triangle meshes can be done using particle filters [9]. Chen et al. introduced a Monte Carlo Localization (MCL) method for meshes, which utilizes LiDARs and OpenGL-simulated range images for importance sampling [10]. However, particle filter-based approaches produce high computational loads to track

<sup>1</sup>Freely available here <https://github.com/uos/rmcl>

the robot's pose. To overcome this issue, relative localization methods such as iterative closest point (ICP) are often used to track the robot's pose [11]–[15]. All of them register a measured point cloud to a reference point cloud. Several publications, spanning from computer graphics to robotics research, have presented ICP-like methods that can register point clouds to reference meshes instead [7], [16]–[20].

In 2019, Mejia-Parra et al. solved point cloud to mesh registration with a novel approach of finding the closest surface point for each point cloud point using hash grids [19]. They evaluated their approach by registering point clouds to single meshes of closed objects. However, dealing with meshes of large environments, as in [10], opens up problems that their approach cannot handle. For example, triangle mesh maps of interiors usually consist of walls with two parallel surfaces. If the initial pose estimate deviates just a little from the optimum, this would lead to matches between wrong wall surfaces. In addition, large meshes would drastically increase the size of the hash table, making it impossible to use on mobile robots. In 2021, Vizzo et al. presented an approach for mesh-based SLAM named PUMA [7]. They generated a mesh from a scan and registered the following scan to it by using ray casting correspondences (RCC). Their correspondences seem to be suitable to solve the mentioned issues of [19]. However, even for fractions of the complete mesh map, they did not achieve real-time capability which makes it infeasible for online operation on autonomous vehicles.

With MICP-L, we address the problems of [7] and [19] by introducing a light-weight, hardware-accelerated method to find RC correspondences and optimize the pose estimation. We reach more than real-time localization even in large-scale mesh maps and overcome convergence issues of classical point cloud-based ICP [21].

### III. MICP-L

MICP-L continuously registers range data acquired from one or multiple range sensors to a triangle mesh map, starting at an initial pose estimate. The general workflow can be summarized as follows:

- 1) Find RC correspondences,
- 2) Estimate the optimal transformation parameters  $\Delta T$  through covariance reduction and SVD,
- 3) Apply  $\Delta T$  to the pose guess and repeat step 1).

#### A. Ray Casting Correspondences

We start with converting each measurement  $i$  of a range sensor into a ray representation, consisting of origin, direction, and range. Next, we use the given pose estimate to trace virtual rays along the paths that the real sensor would scan. The intersection with the map represents the actual point that would be measured if the sensor were at the estimated pose. We then project the Cartesian point of the real scan measurement onto the plane of intersection to determine the map correspondence. These ray casting correspondences (RCC), first introduced in PUMA [7], can match scan points only to the surface closest to the range sensor, as shown in Fig. 2. This reduces the likelihood of

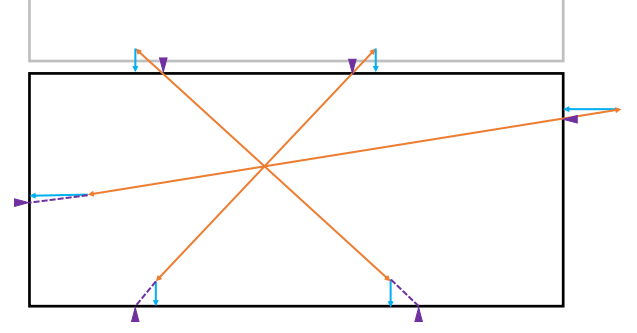


**Fig. 2:** A 2D map consists of two rooms. Conventional correspondence finding methods such as point-to-point and point-to-plane fail since they find correspondences on the wall surface of the wrong room (light gray). With RCC, the real measurement's (orange) correspondences are found using ray casts in the map (purple) and projecting the real measurements onto the intersection plane (blue).

drifting into other rooms during registration as shown in the experiments, subsequently. As a result, RCC generates a list of scan points  $D$  and a list of map points  $M$ , where the  $i$ -th scan point  $d_i$  corresponds to the  $i$ -th map point  $m_i$ .

We use Rmagine, a library to flexibly build ray tracing-based sensor simulations [3], for all ray casts. It allows to decide at run time whether to compute the RCC on its CPU [22] or its NVIDIA GPU [23].

#### B. Correction

Next, we search for the transformation parameters  $\Delta T$ , consisting of a rotation  $\Delta R$  and a translation  $\Delta t$ , that fit the scan points or dataset  $D$  to the map points or model  $M$  best. This can be done by minimizing the following equation:

$$E(\Delta R, \Delta t) = \frac{1}{n} \sum_{i=1}^n \|m_i - (\Delta R d_i + \Delta t)\|_2^2 \quad (1)$$

Once we have the RCCs, we can start to solve for the local optimal solutions for  $\Delta R$  and  $\Delta t$ . Our solver is based on Umeyama's method [24] and enhances the computation of the covariance matrix for both CPU and GPU by transforming it into a reduction operation.

Given two arbitrary partitions of correspondences  $A$  and  $B$  that are used to perform the registration operations  $D_A \rightarrow M_A$  and  $D_B \rightarrow M_B$ . Then  $A$  has the partition parameters  $(\bar{m}_A, \bar{d}_A, \Sigma_A, n_A)$  and  $B$  has the partition parameters  $(\bar{m}_B, \bar{d}_B, \Sigma_B, n_B)$ . Given those parameters, we search for the parameters  $(\bar{m}, \bar{d}, \Sigma, n)$  of the concatenated correspondences by only using the given partition's parameters. We begin with updating the total number of measurements  $n$  and dataset and model means  $\bar{m}, \bar{d}$  by

$$n = n_A + n_B \quad c_A = n_A/n \quad c_B = n_B/n \quad (2)$$

$$\bar{d} = c_A \cdot \bar{d}_A + c_B \cdot \bar{d}_B \quad \bar{m} = c_A \cdot \bar{m}_A + c_B \cdot \bar{m}_B, \quad (3)$$

and then merging the covariances to  $\Sigma$  by

$$\Sigma = c_A \cdot \left( \Sigma_A + (\bar{m}_A - \bar{m})(\bar{d}_A - \bar{d})^T \right) + c_B \cdot \left( \Sigma_B + (\bar{m}_B - \bar{m})(\bar{d}_B - \bar{d})^T \right). \quad (4)$$

From these more general equations, the conventional Umeyama equations can be reconstructed by setting the

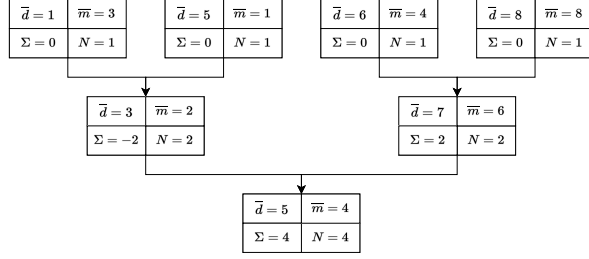


**Fig. 3:** 1D example of covariance reduction given 4 correspondences utilizing Eq. 2-4.

partition  $A$  as the current collection of all correspondences including their mean and covariances beginning with  $(\bar{d}_A, \bar{m}_A, \Sigma_A, n_A) = (0, 0, 0, 0)$ . For every new correspondence  $(d_i, m_i)$  we build a new partition  $B$  with the parameters  $(\bar{d}_B, \bar{m}_B, \Sigma_B, n_B) = (d_i, m_i, 0, 1)$ . After applying equations 2-4, we override the partition parameters of  $A$  with the results and repeat the whole procedure for each new correspondence pair. This gives an exact iterative version analog to the regular two-pass covariance computation method used in [24]. Furthermore, equations 2-4 enable us to create well-balanced CUDA kernels using reductions, as demonstrated in Fig. 3. By applying this to our problem, we can reduce the RCC to two means,  $\bar{d}$  and  $\bar{m}$ , and one covariance matrix  $\Sigma$  per sensor. In our implementation, this is done either on the CPU with OpenMP or on the GPU using CUDA kernels.

If the robot has only one range sensor, we continue with computing the correction parameters  $\Delta R$  and  $\Delta t$  through singular value decomposition (SVD) either using Eigen or CUDA's cuSOLVER according to the original procedure of Umeyama. Depending on whether the calculation is done on the CPU or the GPU, the inputs and outputs are located in CUDA buffers or in the RAM of the CPU, respectively. This allows the development of pre- and post-processing steps where data is transferred between devices only on demand to ensure maximum performance. After correcting the pose guess, we repeat the steps of RCC and correction until convergence. The entire workflow of both the CPU and the GPU correction is shown in Fig. 4.

### C. Combined Correction

Using Umeyama's approach and our modifications, it is feasible to combine multiple range sensors and compute a unified correction. For each sensor  $j$ , we compute the means  $\bar{d}_j$ ,  $\bar{m}_j$ , and covariances  $\Sigma_j$ . Since all correspondences are transformed into a shared coordinate system, we can merge the means and covariances of all sensors with Eq. 2-4. After merging the covariances of individual sensors, we can determine the transformation components to obtain a total correction  $\Delta T$  that contains the influence of every sensor.

Furthermore, we offer the option to replace the automatic calculation of  $c_j$  with user-defined weights to model the impact of certain sensors during correction. If every sensor measurement is equally reliable, we propose selecting the weights based on the number of correspondences, as described in Eq. 2. A sensor with many measurements will automatically

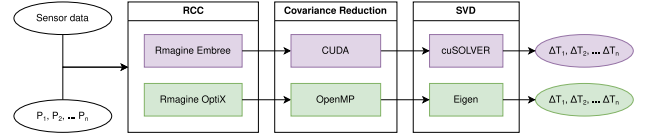


**Fig. 4:** Workflow of MICP-L Correctors. CPU and GPU computations are colored in green and purple respectively. Both the GPU and the CPU implementation receive a list of pose estimates and sensor data. The outputs are delta transforms for each input pose.

have a higher weight assigned to it than a sensor with fewer measurements.

Thus, we enable the correction of multiple sensor sources by merging the intermediate covariances of each sensor. In our implementation, we provide functions to generate a list of partition parameters (one partition per sensor). Additionally, we provide functions to fuse the partitions into one, either uniformly weighted considering the number of measurements or completely user-defined by freely choosing the weights for each sensor. To better understand how they can be combined for correction, consider the following example: We want to localize a robot in a 3D map. This robot is only equipped with a 2D LiDAR, making it difficult to estimate its exact 6DoF pose in the map. However, we know that our robot is on the ground most of the time. We can use this information to attach an additional virtual scanner as Rmagine's OnDn model to the robot that permanently scans from the wheel centers to the ground. This virtual scanner generates fixed distances the size of the wheel radius. Using this virtual scanner and the 2D LiDAR measurements, we can build two covariance matrices for a given pose estimate. The combination of those two is visualized in Fig. 5. Thus, MICP-L can localize a robot equipped with various range sensors. A list of supported configurations is listed in [3].

## IV. EXPERIMENTS

Our experiments aim to analyze our software according to our predefined requirements, as well as to provide a comprehensive overview of its capabilities and limitations.

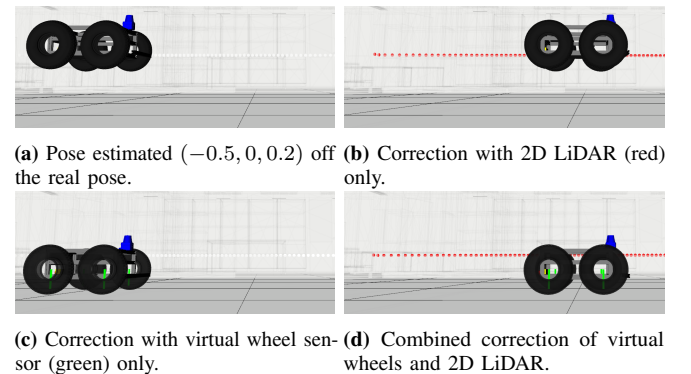


**Fig. 5:** Visualization of a combined correction until convergence. a) shows the pose guess from which the correction starts. It is approximately 0.2 m over the ground (z) and -0.5 m in the x direction of the real pose. b) shows the correction results using only a 2D LiDAR. Here, the robot cannot correct the z error. d) shows the combined correction results considering the single corrections of b) and c) by combining two covariances.





**Fig. 6:** Two test drives in Gazebo AVZ world. The ground truth trajectories are colored in red and blue.

First, we evaluate the localization performance on three challenging real-world domains: agriculture, automotive, and drones. Second, we compare our hardware-accelerated RCC with classic point-to-plane correspondences. Third, we give a detailed overview of MICP-L’s computational demands.

#### A. Localization Performance

Quantifying localization performance necessitates superior localization systems capable of producing precise ground truth data. To mitigate potential errors associated with ground truth estimation, we initially present results obtained from a simulation environment where perfect localization is inherently guaranteed. However, simulations have inherent limitations in terms of realism. Therefore, our second series of experiments focuses on evaluating localization accuracy in real-world datasets.

1) *Simulation:* For our experiments, we used a Gazebo world called AVZ, available in the ROS package `uos_tools`. In this world, we placed a robot equipped with a Velodyne VLP-16 and applied Gaussian noise to the simulated LiDAR data with a standard deviation of 0.8 cm. First, we run MICP-L giving a stationary robot a pose guess near its real position. It converged to a translation error of 0.2 mm. The fact that the error is smaller than the sensor inaccuracy can be justified by the fact that the individual errors average out on the surfaces during registration. In the next experiment, the robot moves through the simulated AVZ environment with a simple, but inaccurate odometry-based pose estimation. MICP-L continuously corrects this estimate to the mesh, and we compared the resulting corrected trajectory to the perfect ground truth provided by Gazebo. For two test drives, the ground truth trajectories, red and blue, are shown in Fig. 6. As a localization metric, we tracked the mean Euclidean distance (MED) to the ground truth trajectory. The odometry resulted in a MED of 8.228 m and 4.5485 m for the red and blue trajectory, respectively. By continuously correcting the odometry using MICP-L, we improved it to 0.98 cm for the red and 0.86 cm for the blue trajectory. This shows that MICP-L is able to correct the inaccurate odometry estimate, achieving an average accuracy of below 1 cm.

2) *Real-world:* To demonstrate the performance of MICP-L in real-world scenarios, we tested our software across various domains, each one providing unique challenges. In agriculture, the environment is particularly unstructured, e.g., parts of the map are constantly changing, like trees moving in the wind or plants growing. The automotive domain includes driving cars with fast translational changes and large

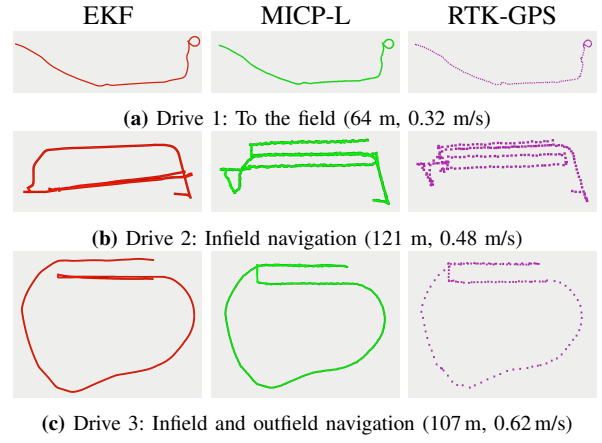


**Fig. 7:** Outdoor experiments: Autonomously navigating the agricultural monitoring robot Lero on a field. For each drive a), b), and c) we recorded the trajectory of the EKF (red), MICP-L (green), and an RTK-GPS (purple).

environments have to be mapped. The drone datasets contain full 6DoF movements, in contrast to the previous domains. Additionally, we selected the drone dataset to specifically assess MICP-L’s performance in GPS-denied environments.

**LERO - Agricultural:** The following experiments investigate MICP-L’s performance in agricultural environments and the integration in the mesh navigation framework [2]. For that, we used the agricultural monitoring robot Lero, which is equipped with an Ouster OS1-64 LiDAR. Lero provides two Intel NUCs, both capable of hardware accelerating MICP-L with RTX GPUs as specified in Tab. II. To build a reference map, we recorded a point cloud of the environment using a Z+F IMAGER 5016 high-resolution terrestrial laser scanner and reconstructed a triangle mesh with LVR2 [5]. The resulting mesh and the robot are shown in Fig. 1. The map consists of 2M triangles and covers an area of  $154 \text{ m} \times 163 \text{ m}$ . It exhibits many beds with a width of about 75 cm, usually 10 m long, and a track width of one meter next to each other. For autonomous robot navigation, we used the Continuous Vector Field Planner (CVP) [2] and the high-level control framework Move Base Flex [25] and recorded three test drives. We observed that in every test drive, Lero was able to robustly navigate across the field and arrive at the given goals precisely, showing that MICP-L synergizes with the CVP. Lastly, we extracted the trajectories estimated by MICP-L, the EKF, and an RTK-GPS module, shown in Fig. 7.

**MulRan - Automotive:** As datasets from the automotive domain, we selected the KAIST sequences of the MulRan datasets [26]. We reconstructed a triangle mesh of the second KAIST sequence using LVR2 [5]. The resulting mesh contains 21,723,560 vertices and 12,408,626 triangles covering an area of  $962 \text{ m} \times 710 \text{ m}$ . For each KAIST sequence, we computed an odometry estimate by using the linear velocity from the GPS data and the orientation from IMU data. With this prior, we ran MICP-L for all three KAIST sequences with three different roughly estimated initial poses but using the same map. The estimated trajectories are shown in Fig. 8. We measured a MED between the MICP-L and ground truth trajectories of 86.65 cm, 61.64 cm, and 60.76 cm for KAIST01,

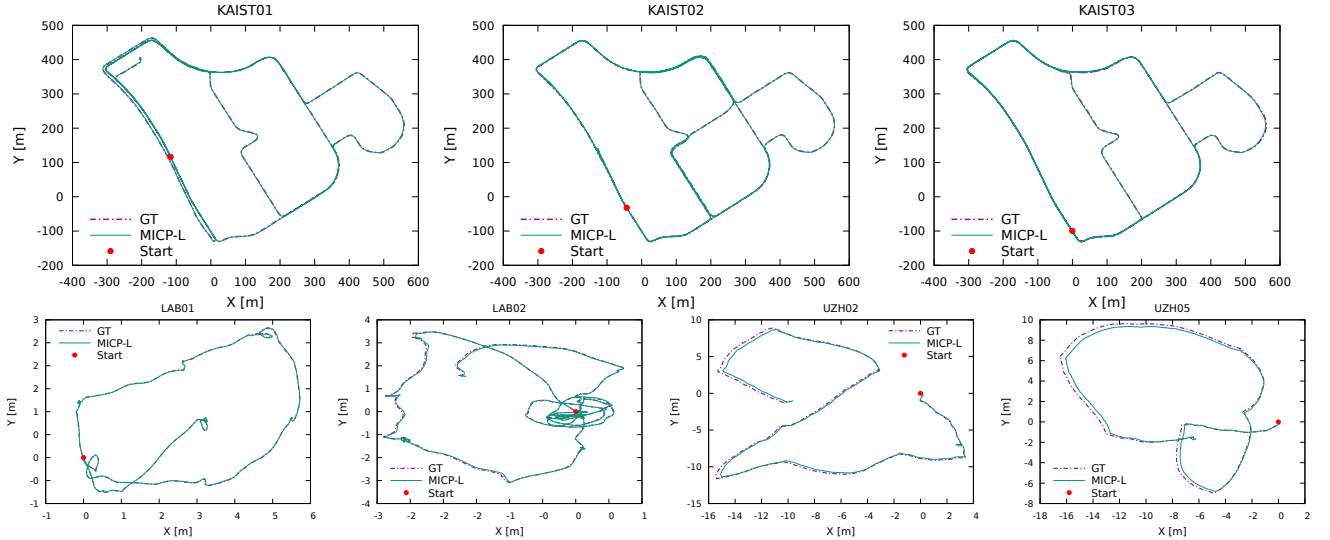


**Fig. 8:** Trajectories estimated by MICP-L. Top row: Localization on MulRan’s KAIST01, KAIST02, and KAIST03 sequence in a map generated by KAIST02 using a GPS/IMU odometry as prior. Bottom row: Localization on Hilti’s LAB01, LAB02, UZH02, and UZH05 sequence in maps generated by LAB02, and UZH05, using IMU as prior.

KAIST02, and KAIST03, respectively. As a second metric, we tracked the rate of valid correspondences (RVC). We define a correspondence of a real scan point with a point on the map to be invalid if their distance is greater than 5 m or the real scan point is outside the range measurable by the sensor. The RVC is then the remaining number of valid points divided by the total number of points and gives a rough estimate of how many points can be considered for registration. In outdoor domains, usually only half of the actual 3D LiDAR measurements can be used, since the other half measures towards the sky and is therefore automatically invalid. So for these cases, the RVC would be around 50 % even for perfect localized robots. On the other hand, once the RVC decreases to a lower value, it normally indicates the robot to be poorly localized. As a third metric, we chose the point-to-mesh error on all valid correspondences (P2M) that measures how accurate a scan is matching the mesh from a given pose estimate, i.e., the actual registration performance. The results are shown in the top part of Tab. I.

The visualization in RViz shows that MICP-L localized the car always successfully relative to the map. However, we observed that the map and ground truth trajectory do not match completely. Yet the low MED and P2M errors show that MICP-L has a high localization accuracy while constantly having low registration errors.

**Hilti - Drone:** In the final experiment, we used the sequences “Lab” (LAB) 1, 2 and “RPG Drone Testing Arena” (UZH) 2, 5 from Hilti SLAM challenge [27], as they contain OS0-64 LiDAR data as well as 6DoF ground truth data from an external motion capture system. We used HATSDF-SLAM [1] to generate mesh maps from UZH02 and LAB02 using the ground truth as prior. In LAB02, we additionally disabled the registration in order to generate the map using the ground truth only. With the IMU of the OS0-64 and applied Madgwick filter, we computed an orientation prior for MICP-L [28] and limited the RCC to a maximum distance

**TABLE I:** Rate of valid correspondences (RVC) and the mean point-to-mesh distance (P2M) of ground truth and MICP-L trajectory on the Hilti and MulRan datasets.

|        | Sequence | GT      |           | MICP-L         |                 |
|--------|----------|---------|-----------|----------------|-----------------|
|        |          | RVC     | P2M       | RVC            | P2M             |
| MulRan | KAIST01  | 41.66 % | 48.51 cm  | <b>43.76 %</b> | <b>19.57 cm</b> |
|        | KAIST02  | 41.47 % | 79.44 cm  | <b>46.94 %</b> | <b>16.68 cm</b> |
|        | KAIST03  | 36.60 % | 117.31 cm | <b>46.32 %</b> | <b>15.74 cm</b> |
| Hilti  | LAB02    | 100.0 % | 4.7 cm    | 100.0 %        | <b>4.4 cm</b>   |
|        | LAB01    | 100.0 % | 6.0 cm    | 100.0 %        | <b>5.2 cm</b>   |
|        | UZH02    | 100.0 % | 11.9 cm   | 100.0 %        | <b>3.6 cm</b>   |
|        | UZH05    | 100.0 % | 10.1 cm   | 100.0 %        | <b>3.5 cm</b>   |

of 0.5 m. We then ran MICP-L on LAB02 and UZH02 as well as on LAB01 and UZH05. The estimated trajectories are shown in Fig. 8. Again, we tracked the MED between ground truth and MICP-L trajectories. In average, we measured errors of 2.2 cm, 1.0 cm, 21.5 cm, and 22.3 cm for LAB02, LAB01, UZH02, and UZH05, respectively. An issue with HATSDF-SLAM’s TSDF approach is that cells can be overwritten during mesh generation. As a result, the mapping process produces accurate 3D maps but does not guarantee that the map exactly matches the ground truth, i.e., measuring the MED alone would not be meaningful. Accordingly, we chose the RVC and P2M as second metrics to measure the actual registration performance. The averaged P2M for both the ground truth and MICP-L are shown in the bottom part Tab. I. On Hilti datasets, all RVC scores are 100 % since the map is a closed surface and a scan point never exceeds the limit 5 m from the mesh.

For UZH we measured high trajectory errors, but low point-to-mesh errors. At frame 150 of UZH02 the MDE and GT P2M rises, while the MICP-L P2M remains at low errors. Similar effects were observed in UZH05 and both LAB sequences probably due to a map that diverges too far from the ground truth trajectory or imprecise ground truth measurements in space or time. Therefore, the lower MEDs observed when running MICP-L on the LAB sequences

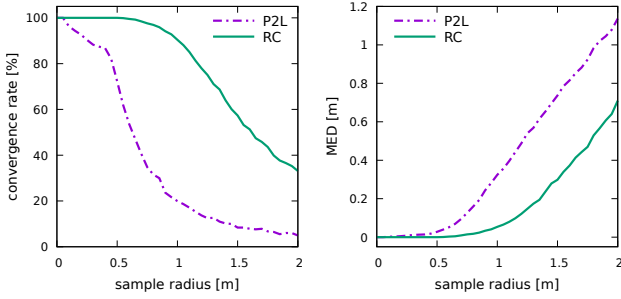


**Fig. 9:** Convergence rates (left) and total translation errors (right) of ray casting (RC) correspondences and classic point-to-plane (P2L) correspondences in AVZ map Fig. 6.

**TABLE II:** Computers used for run time evaluation.

| Name | CPU               | GPU                      |
|------|-------------------|--------------------------|
| DPC  | AMD Ryzen 7 3700X | NVIDIA RTX 2070 SUPER    |
| NUC  | Intel i7 1165G7   | NVIDIA RTX 2060 Max-P    |
| LX1  | Intel i7 8750H    | NVIDIA GTX 1050 Ti Max-Q |

are attributed to the fact that the map was generated solely from the ground truth trajectory. This indicates that the map generated from *UZH02* diverged too far from ground truth with HATSDF-SLAM. On the *LAB* sequences we also observed that the ground truth trajectories produce larger point-to-mesh errors than our approach. The reported MICP-L P2M errors are close to the OS0-64 noise of  $\pm 3$  cm.

### B. Convergence Study

We compared our hardware-accelerated RCCs with state-of-the-art point-to-plane (P2L) correspondences by measuring the convergence rate and registration accuracy for both correspondence types on the AVZ map. In the experiment, we placed a virtual robot in the center of a room and simulated a Velodyne VLP-16 scan. Then, we drew 512 random positions from a circular uniform distribution around the actual position of the robot. Together with an unchanged orientation, these random positions serve as initial guesses for registration. After 50 iterations using either RC or P2L as correspondences, we measured the rate of successful convergence as well as the MED of each estimated pose to the actual robot pose. This experiment was repeated in every room. We tracked the MED and convergence rates while increasing the radius of the uniform sample distribution. The averaged results over all rooms are shown in Fig. 9.

### C. Computational Demands

First, we analyze the run time of our GPU and CPU implementation, considering varying map sizes, and different computing devices. The computers used in experiments are listed in Tab. II. For each of the experiments shown in Fig. 10, we measured the run time for a Velodyne VLP-16 LiDAR as a virtual sensor. The VLP-16 has 16 scan lines and operates with frame rates up to 20 Hz. In the horizontal direction, the number of points is adjustable. In our experiments, we used 900 horizontal points, requiring the calculation of 14,400

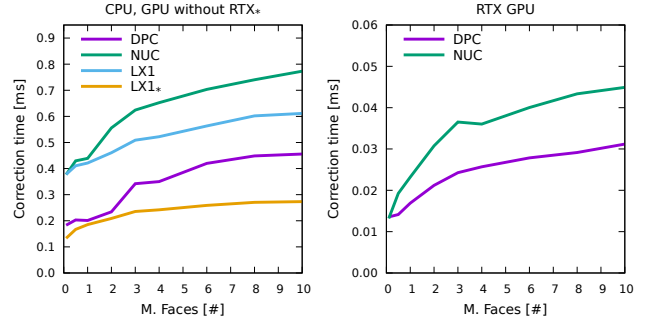


**Fig. 10:** Run time evaluation of a single MICP-L iteration in synthetic maps of varying sizes on different architectures for CPUs and GPUs without (left) and with RTX capabilities (right).

**TABLE III:** MICP-L partial run times for CPU, non-RTX-GPU (GPU), and RTX-GPU (RTX) devices.

| Device | Simulation | Reduction | SVD      |
|--------|------------|-----------|----------|
| CPU    | 96.400 %   | 3.586 %   | 0.014 %  |
| GPU    | 94.090 %   | 0.014 %   | 5.896 %  |
| RTX    | 80.337 %   | 0.376 %   | 19.287 % |

RCCs. Next, we spawned 1,000 random pose guesses inside an automatically generated sphere and simulated a VLP-16 scan at the sphere’s center. Afterwards, we used MICP-L to register this scan from each pose estimate against the sphere, so that every random pose estimate converges at the center of the sphere. We measured the run times per correction step for different numbers of sphere triangles on all devices listed in Tab. II. The results are summarized in Fig. 10. The experiments show that our proposed algorithm is online capable in 3D maps consisting of many triangles. With the Intel NUC’s RTX acceleration, a VLP-16 scan is corrected about 850,000 times in a map of 1 million faces between two scans.

In a second experiment, we measured each component of MICP-L (Fig. 4) for all considered devices by spawning a sphere consisting of 1M faces and registering 1,000 poses against the mesh. The results in Tab. III provide an overview of how much time each fraction of the correction needs in relation to the entire computation.

## V. CONCLUSION

We presented MICP-L, an approach to robustly localize a robot equipped with one or more range sensors in triangle mesh maps. MICP-L is specifically designed for robotic applications, due to its compatibility with arbitrary combinations of arbitrary range sensors. Our method was evaluated in terms of robust localization performance across the domains of agriculture, drones, and automotive applications. Furthermore, it was successfully integrated with state-of-the-art software for mesh navigation. The required computational steps can be flexibly distributed to both CPU and GPU, making our method adaptable to diverse robotic platforms and target architectures. With our hardware-accelerated approach to finding RCCs, we gain significant advantages over classic point-to-plane correspondences in terms of runtime, convergence rate and registration accuracy.

## REFERENCES

- [1] M. Eisoldt, M. Flottmann, J. Gaal, P. Buschermöhle, S. Hinderink, M. Hillmann, A. Nitschmann, P. Hoffmann, T. Wiemann, and M. Porrmann, "HATSDF SLAM – Hardware-accelerated TSDF SLAM for Reconfigurable SoCs," in *European Conference on Mobile Robots (ECMR)*. IEEE, 2021, pp. 1–7.
- [2] S. Pütz, T. Wiemann, M. Kleine Piening, and J. Hertzberg, "Continuous Shortest Path Vector Field Navigation on 3D Triangular Meshes for Mobile Robots," in *International Conference on Robotics and Automation (ICRA)*. IEEE, 2021, pp. 2256–2263.
- [3] A. Mock, T. Wiemann, and J. Hertzberg, "Rmagine: 3D Range Sensor Simulation in Polygonal Maps via Raytracing for Embedded Hardware on Mobile Robots," in *International Conference on Robotics and Automation (ICRA)*. IEEE, 2023, pp. 9076–9082.
- [4] J. Ruan, B. Li, Y. Wang, and Y. Sun, "SLAMesh: Real-time LiDAR Simultaneous Localization and Meshing," in *International Conference on Robotics and Automation (ICRA)*. IEEE, 2023, pp. 3546–3552.
- [5] T. Wiemann, I. Mitschke, A. Mock, and J. Hertzberg, "Surface Reconstruction from Arbitrarily Large Point Clouds," in *International Conference on Robotic Computing (IRC)*. IEEE, 2018, pp. 278–281.
- [6] A. Dai, M. Nießner, M. Zollhöfer, S. Izadi, and C. Theobalt, "BundleFusion: Real-Time Globally Consistent 3D Reconstruction Using On-the-Fly Surface Reintegration," *ACM Transactions on Graphics (ToG)*, vol. 36, no. 4, p. 1, 2017.
- [7] I. Vizzo, X. Chen, N. Chebrolu, J. Behley, and C. Stachniss, "Poisson Surface Reconstruction for LiDAR Odometry and Mapping," in *International Conference on Robotics and Automation (ICRA)*. IEEE, 2021, pp. 5624–5630.
- [8] J. Lin, C. Yuan, Y. Cai, H. Li, Y. Zou, X. Hong, and F. Zhang, "ImMesh: An Immediate LiDAR Localization and Meshing Framework," *arXiv preprint arXiv:2301.05206*, 2023.
- [9] M. Dreher, H. Blum, R. Siegwart, and A. Gawel, "Global Localization in Meshes," in *International Symposium on Automation and Robotics in Construction (ISARC)*, vol. 38. IAARC, 2021, pp. 747–754.
- [10] X. Chen, I. Vizzo, T. Labe, J. Behley, and C. Stachniss, "Range Image-based LiDAR Localization for Autonomous Vehicles," in *International Conference on Robotics and Automation (ICRA)*. IEEE, 2021, pp. 5802–5808.
- [11] S. Rusinkiewicz and M. Levoy, "Efficient Variants of the ICP Algorithm," in *International Conference on 3-D Digital Imaging and Modeling (3DIM)*. IEEE, 2001, pp. 145–152.
- [12] K. Koide, M. Yokozuka, S. Oishi, and A. Banno, "Voxelized GICP for Fast and Accurate 3D Point Cloud Registration," in *International Conference on Robotics and Automation (ICRA)*. IEEE, 2021, pp. 11 054–11 059.
- [13] T. Shan and B. Englot, "LeGO-LOAM: Lightweight and Ground-Optimized Lidar Odometry and Mapping on Variable Terrain," in *International Conference on Intelligent Robots and Systems (IROS)*. IEEE, 2018, pp. 4758–4765.
- [14] T. Shan, B. Englot, D. Meyers, W. Wang, C. Ratti, and R. Daniela, "LIO-SAM: Tightly-coupled Lidar Inertial Odometry via Smoothing and Mapping," in *International Conference on Intelligent Robots and Systems (IROS)*. IEEE, 2020, pp. 5135–5142.
- [15] A. Segal, D. Haehnel, and S. Thrun, "Generalized-ICP," in *Robotics: science and systems (RSS)*, 2009.
- [16] D. Holz and S. Behnke, "Registration of Non-Uniform Density 3D Point Clouds using Approximate Surface Reconstruction," in *International Symposium on Robotics (ISR)*. VDE, 2014, pp. 1–7.
- [17] W. Li and P. Song, "A modified ICP algorithm based on dynamic adjustment factor for registration of point cloud and CAD model," *Pattern Recognition Letters*, vol. 65, pp. 88–94, 2015.
- [18] A. Avetisyan, M. Dahnert, A. Dai, M. Savva, A. X. Chang, and M. Nießner, "Scan2CAD: Learning CAD Model Alignment in RGB-D Scans," in *Conference on Computer Vision and Pattern Recognition (CVPR)*. IEEE, 2019, pp. 2614–2623.
- [19] D. Mejia-Parra, J. Lalinde-Pulido, J. R. Sánchez, O. Ruiz-Salguero, and J. Posada, "Perfect Spatial Hashing for Point-cloud-to-mesh Registration," in *CEIG*. The Eurographics Association, 2019, pp. 41–50.
- [20] P. Bourquart, D. Coeurjolly, G. Damiand, and F. Dupont, "Hierarchical mesh-to-points as-rigid-as-possible registration," *Computers & Graphics*, vol. 102, pp. 320–328, 2022.
- [21] J. Zhang, Y. Yao, and B. Deng, "Fast and Robust Iterative Closest Point," *IEEE Transactions on Pattern Analysis and Machine Intelligence*, vol. 44, no. 7, pp. 3450–3466, 2022.
- [22] I. Wald, S. Woop, C. Benthin, G. S. Johnson, and M. Ernst, "Embree: A Kernel Framework for Efficient CPU Ray Tracing," *ACM Transactions on Graphics (TOG)*, 2014.
- [23] S. G. Parker, J. Bigler, A. Dietrich, H. Friedrich, J. Hoberock, D. Luebke, D. McAllister, M. McGuire, K. Morley, A. Robison, and M. Stich, "OptiX: A General Purpose Ray Tracing Engine," *ACM Transactions on Graphics (TOG)*, 2010.
- [24] S. Umeyama, "Least-squares estimation of transformation parameters between two point patterns," *IEEE Pattern Analysis & Machine Intelligence (PAMI)*, vol. 13, no. 04, pp. 376–380, 1991.
- [25] S. Pütz, J. S. Simón, and J. Hertzberg, "Move Base Flex: A Highly Flexible Navigation Framework for Mobile Robots," in *International Conference on Intelligent Robots and Systems (IROS)*. IEEE, 2018, pp. 3416–3421.
- [26] G. Kim, Y. S. Park, Y. Cho, J. Jeong, and A. Kim, "MulRan: Multimodal Range Dataset for Urban Place Recognition," in *International Conference on Robotics and Automation (ICRA)*. IEEE, 2020, pp. 6246–6253.
- [27] M. Helmberger, K. Morin, B. Berner, N. Kumar, G. Cioffi, and D. Scaramuzza, "The Hilti SLAM Challenge Dataset," *IEEE Robotics and Automation Letters (RAL)*, vol. 7, no. 3, pp. 7518–7525, 2022.
- [28] S. Madgwick *et al.*, "An efficient orientation filter for inertial and inertial/magnetic sensor arrays," *Report x-io and University of Bristol (UK)*, 2010.